

Aerodynamic Impacts of Helicopter Blade Erosion Coatings

Mark E. Calvert,¹ and Tin-Chee Wong.²

*Aviation and Missile Research, Development and Engineering Center,
United States Army Research, Development and Engineering Command,
Redstone Arsenal, AL, 35898-5000.*

The United States Army helicopter fleet experiences deformation of rotor blade contours from sand erosion and the implementation of technologies to protect against it. An investigation was performed to determine the effect of a typical erosion protection coating on the main rotor performance of a UH-60A Blackhawk utility helicopter. Computational fluid dynamics was used to calculate aerodynamic coefficients for representative coated airfoil sections. Hover analyses were performed to evaluate the impact of the coated airfoils on main rotor performance. The results show that airfoil erosion protection coatings can cause a decrease in the rotor's aerodynamic efficiency.

Nomenclature

C	=	chord length, ft.
c_d	=	section drag coefficient
c_{d0}	=	section drag coefficient at zero lift
CFD	=	computational fluid dynamics
c_l	=	section lift coefficient
C_P	=	power coefficient
C_T	=	thrust coefficient
FM	=	figure of merit
$NACA$	=	National Advisory Committee on Aeronautics
R	=	rotor radius
SLS	=	sea level standard atmospheric conditions
X	=	airfoil ordinate in the chord-wise direction
y^+	=	dimensionless, sublayer-scaled, distance
Z	=	airfoil ordinate normal to the chord
α	=	angle of attack, deg
σ	=	rotor solidity

I. Introduction

SURFACE erosion from sand presents a significant challenge to helicopter rotor blades. Metallic leading-edge abrasion strips made from nickel, titanium and stainless steel provide good protection against precipitation, but suffer excessive wear against sand. Polymer-based coatings have gained popularity as an expeditious method of protecting blades against sand erosion, and often offer the added benefit of being field repairable. However, most polymer-based coatings provide poor protection against precipitation-induced erosion, the area where metal abrasion strips excel. The net result is that polymer-based coated blades are used in areas where sand erosion is a problem, and not in regions where precipitation is the dominant erosion factor.

Polymer-based erosion coatings are usually applied to helicopter rotor blades after manufacture, and often after the blades have been fielded. Application of the polymer usually involves masking sections of the rotor blade behind the leading edge and then applying the coating. After the coating has dried, the masking material is removed. Unless further finishing processes are applied, this results in a discontinuous edge between the coated and uncoated sections of the blade, usually in the form of a rearward facing step. Thus, the helicopter in the field operates with off-design airfoil contours on the protected sections of the blades.

¹ Aerospace Engineer, Aviation Engineering Directorate, RDMR-AEA, AIAA Senior Member.

² Aerospace Engineer, Aviation Engineering Directorate, RDMR-AEA, AIAA Senior Member.

The National Advisory Committee on Aeronautics (NACA) conducted several studies of the influence of airfoil contour variation on aerodynamic performance during the 1930s and 40s. Ward¹ investigated the effect of minor contour variation on airfoil aerodynamic performance. Ward compared two versions of the Göttingen 387 airfoil, one constructed from ordinates from the Göttingen laboratory (Göttingen 387-G), and one constructed from ordinates from NACA (Göttingen 387). The variation between the two profiles was within one-half percent of the chord length. Results from wind tunnel tests showed a 4.5 percent difference in maximum lift, an 8.0 percent difference in minimum profile drag, and a 3.5 percent difference in the lift-to-drag ratio. Ward also compared the NACA 100 and the NACA 0021 symmetrical airfoils as representative of the difference observed between airfoil ordinates from different laboratories. For this case, the physical variation between the two airfoil sections was less than one-quarter percent of the chord length. The wind tunnel tests showed a 9.4 percent difference in maximum lift and a 2.3 percent difference in the lift-to-drag ratio.

In 1934, Jacobs² investigated the effects of protuberance on airfoil section aerodynamic coefficients. He found that protuberances as small as one thousandth of the chord length forward of the maximum thickness location could cause a significant increase in airfoil drag. Fairing was found to reduce the drag, but did not eliminate it. The maximum airfoil lift coefficient was also found to be significantly reduced by protuberances of the size of a typical aircraft wing's surface roughness. Jacobs³ extended his research to include the effect of protuberances on wings. He found that protuberance of short span could cause a reduction in a wing's maximum lift, but that fairing the protuberances could mitigate this effect.

Other researchers^{4,5,6} have investigated the effects of environmental roughness on airfoil aerodynamic performance. These effects include rain, insect deposits and ice accretion. Wetted airfoils have been shown to have a 30 percent reduction in lift for torrential rain conditions. Insect impacts on airfoil sections can act as distributed roughness. The equivalent sand roughness of the surface is dependent on the predominant species of insect, and the speed at which insects impact the airfoil. The effect of ice accretion is dependent on the thickness of the ice on the airfoil. The predominant results of these investigations are that even minor variations in airfoil surface contour within the leading 5 percent of the chord length can cause significant changes in aerodynamic performance, areas that will typically encounter the greatest sand erosion, thus requiring the greatest protection. The purpose of this paper is to report work performed to evaluate the aerodynamic impact of leading edge blade erosion coatings on helicopter main rotor performance.

II. Airfoil Performance

The SC1095 airfoil section⁷ that comprises the majority of the UH-60A Blackhawk main rotor blade span was used to evaluate the aerodynamic performance impact of a representative erosion protective coating application. Two representative coated airfoil geometries were evaluated. The first used a sharp, backward-facing step for the condition that the erosion protection coating terminated cleanly at the termination point (the "Step" profile, Figure 1). The second airfoil geometry included a rounded "bump," to simulate the case where the coating might slightly overlap the masking material used during the coating process (the "Bump" profile, Figure 2). Both protective coatings terminated at 20 percent of the airfoil chord behind the leading edge on both the top and bottom surfaces. The coating thickness was taken as 0.120 percent of the chord length. (This is equivalent to a coating applied at 25 mil thickness to an airfoil with a 20.76 inch chord, typical of the majority of the span for the UH-60A main rotor.)

In addition to the Step and the Bump geometries, the standard SC1095 airfoil contour was included in the analysis (the "Clean" profile) as the baseline for comparison purposes.

A. Methodology

The aerodynamic performance of the three airfoil profiles were evaluated through Computational Fluid Dynamics simulations (CFD). Following the methodologies described in Reference⁸, the unstructured Navier-Stokes solver FUN3D⁹ was used for the calculations. FUN3D uses an implicit, upwind, finite-volume discretization in which the dependent variables are stored as mesh vertices. Inviscid fluxes at cell interfaces were computed using the flux-differencing scheme of Roe and viscous fluxes were evaluated by using an approach equivalent to a central-difference Galerkin procedure. For steady-state flows, temporal discretization was performed by using a backward Euler time-stepping scheme. At each time step, the linear system of equations was approximately solved with an implicit line relaxation scheme. A local time-step technique was employed to accelerate convergence to steady-state solution. For all results presented in this paper, the flow was assumed to be fully turbulent. The one-equation

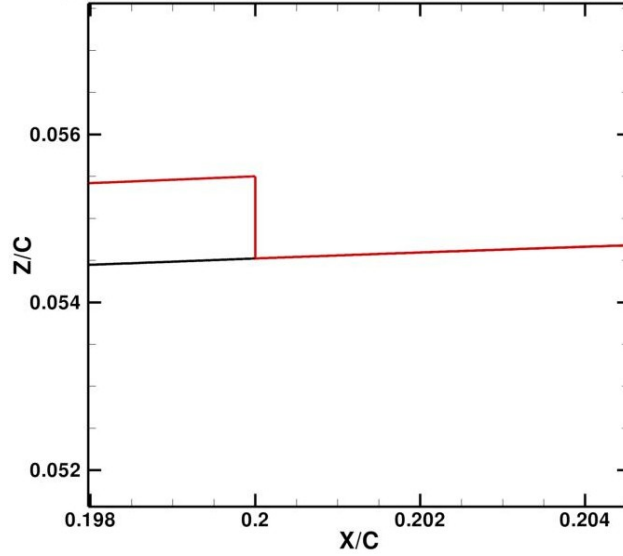


Figure 1. Magnified image of the sharp rearward-facing ledge on the “Step” SC1095 airfoil.

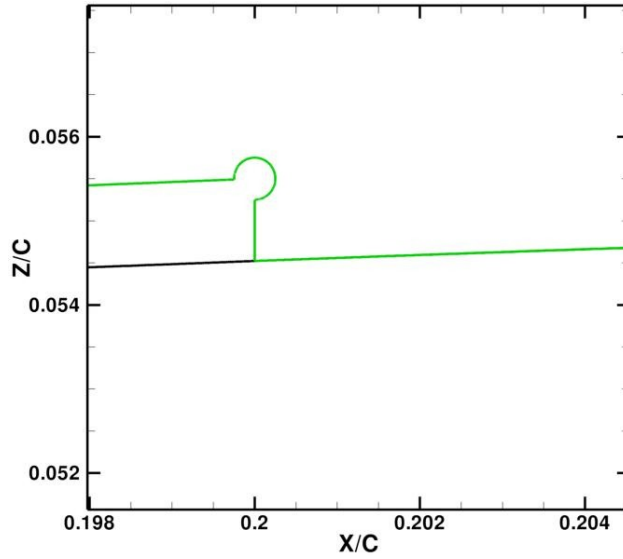


Figure 2. Magnified image of the rearward-facing ledge with bump on the “Bump” SC1095 airfoil.

turbulence model of Spalart and Allmaras was employed and solved in a loosely coupled fashion. The simulations were run until the L_2 norm of the density residual dropped by six orders of magnitude, which usually required roughly 2000 steps to achieve.

The computational mesh around the airfoils consisted of 6.69×10^5 nodes. The surface of the Clean and the Step contours were discretized with 3,345 nodes. The Bump contour required 19 additional points to discretize the rounded bumps, for a total of 3,364 nodes on the surface. The minimum spacing of the grid above the airfoil surface was specified as 1×10^{-6} chord to assure that the first layer of cells above the airfoil surface were within the dimensionless distance $y^+ = 1$. The outer boundary was placed at 20 chord diameters away from the airfoil surface, and was discretized with 200 points. A point vortex boundary condition was used on the outer boundary to minimize the distance to the outer boundary. Figure 3 shows a plot of the computational mesh used for the clean SC1095

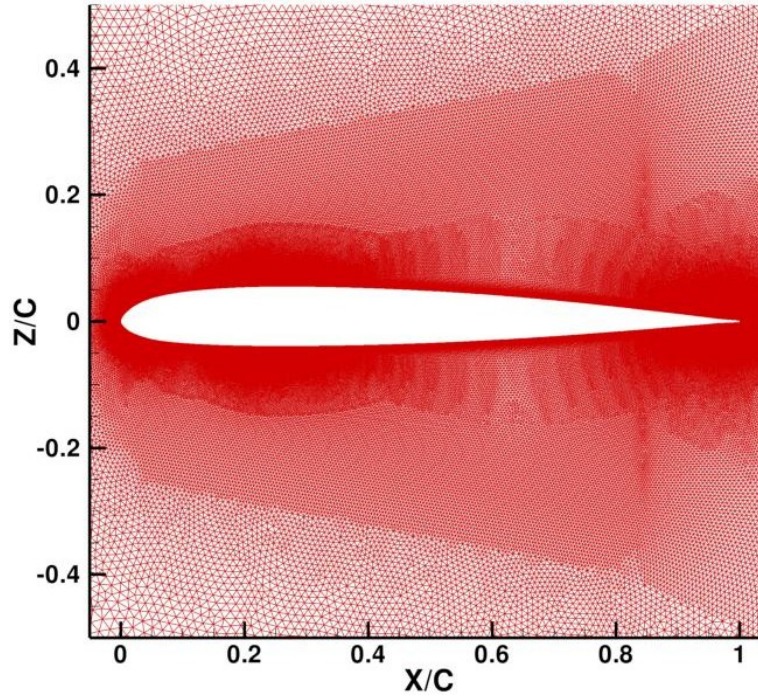


Figure 3. Computational grid showing the Clean SC1095 airfoil contour.

airfoil contour. Meshes for the Step and Bump profiles are not shown due to the small size of the coating thickness relative to the total airfoil length.

The results from the CFD simulations were used to populate tables of nondimensional lift, drag and moment coefficients for the three airfoil profiles. Mach numbers (Ma) values were specified as 0.30, 0.40, 0.50, 0.61, 0.74, 0.82, and 0.92. The Mach 0.30 condition coefficient values were copied to expand the table to 0.00 Mach number. The 0.92 Mach number coefficient values were copied to extend the tables to 1.00 Mach number. The angle of attack (α) range was varied from -180 to +180 degrees, in 5 degree increments, except for the range of -5 to 25 degrees, where a 1 degree sweep increment was specified. Reynolds number based on grid length was specified as 4×10^6 for the Mach 0.30 condition. Reynolds number was linearly increased by 1×10^6 for each 0.1 increase in Mach number.

Validation of this methodology was assumed due to similarity to the calculations described in Reference 8.

B. Results and Discussion

Figures 4 through 6 show nondimensional aerodynamic coefficient results from the CFD simulations for the Mach 0.30 condition in the angle of attack span including the linear region and the maximum lift coefficient. Figure 4 shows that the lift-curve slopes of the three profiles overlie in the linear region and begin to diverge slightly near maximum lift and beyond. The maximum lift coefficient for both the Step and the Bump profiles are approximately 2 percent smaller than the Clean profile. Over the angle of attack range shown, the Step and Bump profile lift coefficients are not discernibly different from each other until the airfoils reach maximum lift and begin to stall.

Figure 5 shows the nondimensional drag as a function of angle of attack. For this coefficient, the drag for the Step and Bump profiles are significantly larger than the Clean profiles over the range shown. The zero lift drag (c_{d0}) is roughly 1.4 counts larger for the Step and Bump profiles than for the Clean profile. Also, the difference in drag between the Clean and the other two profiles is significantly increased between 5 and 13 degrees, above which points the drag plots are roughly converged again in the post-stall region. By comparing the differences shown in Figure 4 to differences shown in Figure 5, it may be seen that the largest change in aerodynamic performance results from the increase in profile drag of the coated airfoils, rather than a significant reduction in lift capability for Mach 0.30.

Figure 6 shows plots of lift-to-drag ratio (L/D) versus angle of attack. From this plot, it may be seen that the Clean airfoil achieves its greatest aerodynamic efficiency at an angle of attack of 8.3 degrees, with a L/D value of

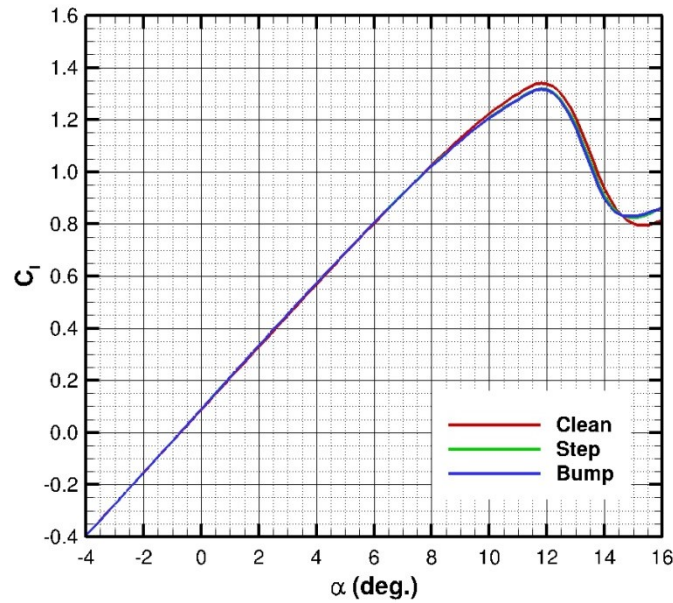


Figure 4. Lift coefficient versus angle of attack for Mach 0.30.

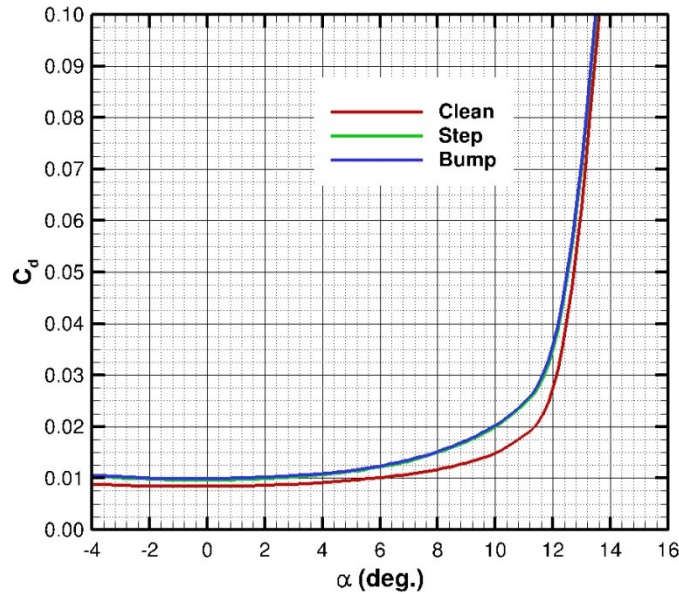


Figure 5. Drag coefficient versus angle of attack for Mach 0.30.

88. The Step airfoil achieves a maximum L/D value of 70 at 7 degrees, while the Bump airfoil reaches a maximum L/D value of 68 at 7.4 degrees. It may be noted from this figure that not only has the total aerodynamic efficiency of the coated airfoils been reduced, as denoted by the decrease in lift-to-drag ratio, but the angle of attack for maximum lift efficiency occurs earlier by approximately 1 degree, thus compounding the power penalty caused by the presence of the coating under the maximum lift conditions.

To further examine the differences in the aerodynamic behavior between the Clean and coated airfoils, Figures 7 through 9 show flowfield results on the suction side of the three airfoil sections for a 5 degree angle of attack at a

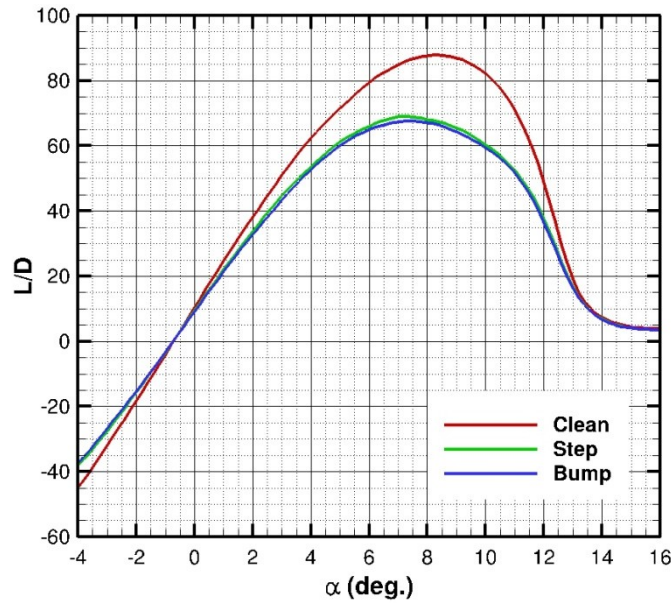


Figure 6. Lift-to-drag ratio versus angle of attack for Mach 0.30.

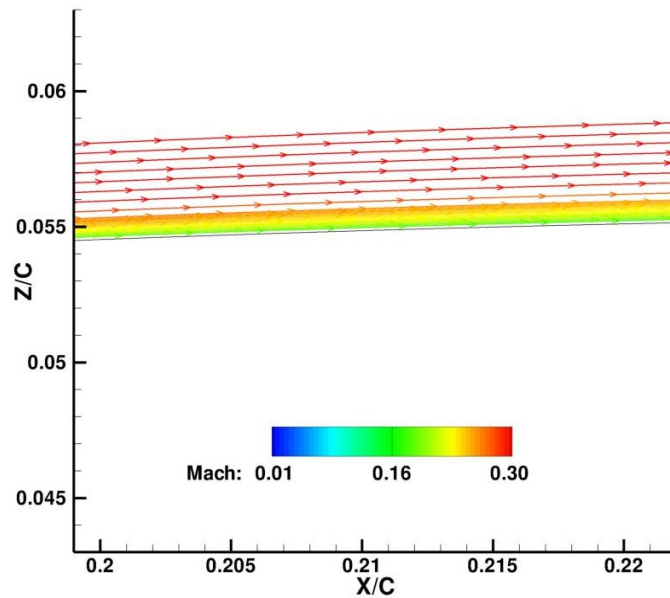


Figure 7. Streamlines for the Clean airfoil at a 5° angle of attack.

freestream Mach number of 0.30. Figure 7 shows stream lines for the Clean airfoil, where the flow remains attached. Figure 8 shows streamlines for the Step airfoil, where the presence of the backward-facing step creates a small recirculation cell. Figure 9 shows streamlines for the Bump airfoil, where the addition of the rounded bump profile at the top of the ledge produces a larger recirculation cell than the Step airfoil. The flows reattach behind the recirculation cells for both coated airfoil cases, but the following boundary layer thickness is increased compared to the Clean airfoil. These net changes in flow behavior result in increases in profile drag for the 5 degree cases at Mach 0.30.

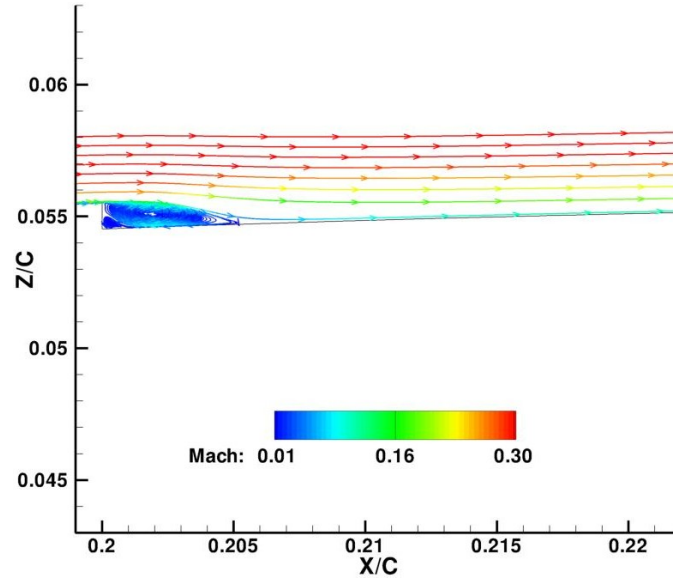


Figure 8. Streamlines for the Step airfoil at a 5° angle of attack.

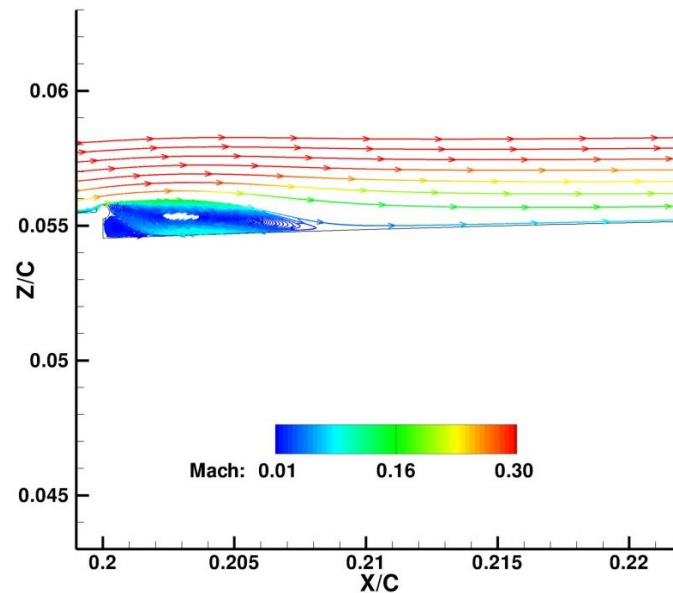


Figure 9. Streamlines for the Bump airfoil at a 5° angle of attack.

Figures 10 through 12 show nondimensional aerodynamic coefficient results from the CFD simulations for the Mach 0.61 condition in the angle of attack span, including the linear region and the maximum lift coefficient. Figure 10 shows that the lift-curve slopes of the three profiles overlie in the linear region and begin to diverge near 4.5 degrees, slightly before maximum lift and then beyond. For this condition, the maximum lift coefficients for the Step and Bump airfoils are approximately 2 percent larger than the Clean airfoil, and occurs approximate 0.5 degree earlier than the Clean airfoil. Over the angle of attack range shown, the Step and Bump profile lift coefficients are again not discernibly different from each other until the airfoils reach maximum lift and begin to stall.

Figure 11 shows the nondimensional drag as a function of angle of attack. For this coefficient, the drag for the Step and Bump profiles are larger than the Clean profiles over distinct intervals in angle of attack. The zero lift drag (c_{d0}) is slightly smaller than 1 count for the Step and Bump profiles than for the Clean profile. In addition, the difference in drag between the Clean and the other two profiles is significantly increased between 0.2 and 4.5 degrees, above which points the drag plots roughly intertwine in the post-stall region.

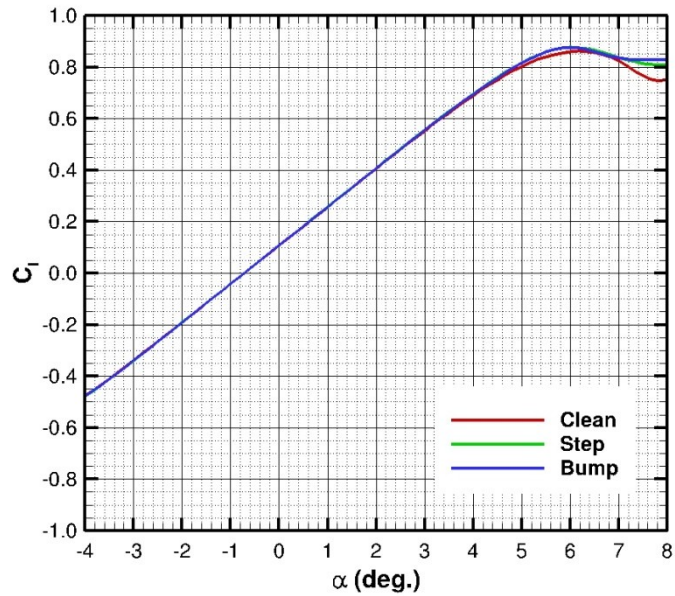


Figure 10. Lift coefficient versus angle of attack for Mach 0.61.

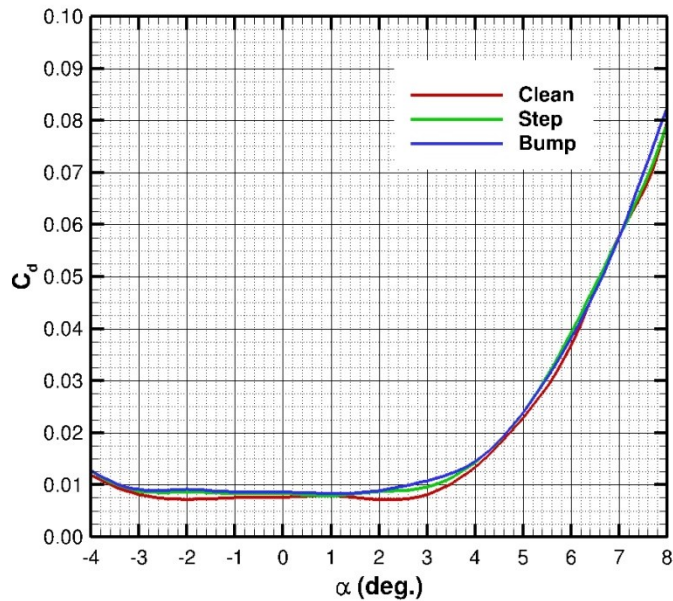


Figure 11. Drag coefficient versus angle of attack for Mach 0.61.

Figure 12 shows plots of lift-to-drag ratio (L/D) versus angle of attack. From this plot, it may be seen that the Clean airfoil achieves its greatest aerodynamic efficiency at an angle of attack of 2.9 degrees, with a L/D value of 64. The Step airfoil achieves a maximum L/D value of 58 at 3 degrees, while the Bump airfoil reaches a maximum L/D value of 51 at 3.1 degrees. As opposed to the Mach 0.30 condition, the aerodynamic efficiency of the coated airfoils occurs earlier than the Clean airfoil by roughly 0.1 degree. While L/D is smaller for the coated cases, by approximately 10 and 15 for the Step and Bump airfoils, respectively, the maximum efficiency does occur at roughly the same angle of attack for all three airfoil sections.

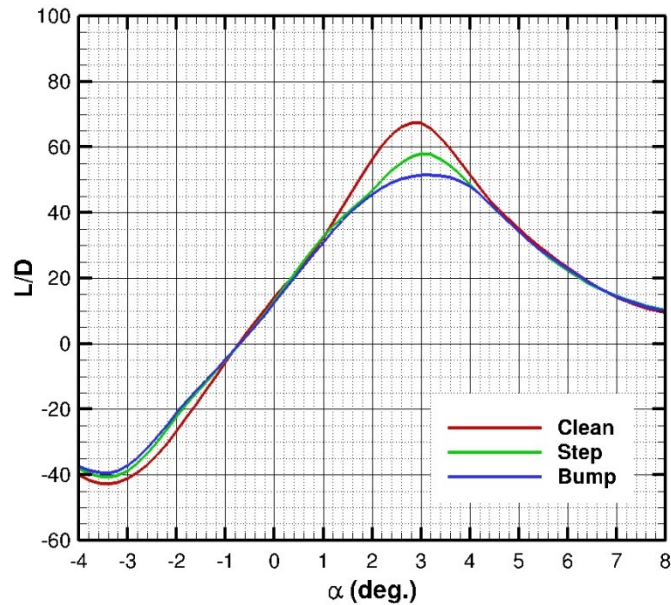


Figure 12. Lift-to-drag ratio versus angle of attack for Mach 0.61.

By considering the Mach 0.30 and 0.61 conditions together, it may be observed that the impact on aerodynamic performance by the erosion coatings is largely confined to increasing the profile drag of the coated airfoils. Changes in maximum lift coefficient are largely insignificant when compared to the changes in the drag coefficient. However, when combined as shown by the plots of lift-to-drag ratio, the changes in lift coefficient and drag coefficient cause a significant reduction in the aerodynamic efficiency of the coated airfoil sections in the angle of attack range approaching maximum lift capability. The Step airfoil also showed a significant increase in aerodynamic efficiency than the Bump airfoil for the Mach 0.61 condition, while the efficiencies were roughly the same for the Mach 0.30 condition. This may be due to the presence of a shock on the leading edge of the airfoil inducing flow separation ahead of the termination point on the coated blades.

III. Integrated Rotor Performance

A hover analysis was performed to evaluate differences in integrated performance of an isolated UH-60A main rotor using the three SC1095 airfoil sections. The LSAF, ver. 2.00, axial flight and hover analysis software¹⁰⁻¹³ from Computational Methodology Associates was used for this evaluation. LSAF uses a lifting surface method to calculate the lift generated by rotor blades. A circulation-coupled prescribed wake model is used to calculate the wake induced velocities at the rotor blade. Drag is calculated through strip-analyses using airfoil table look-ups. LSAF has been shown to accurately predict the hover performance over a wide range of conditions and thrust levels for a variety of isolated rotors and rotorcraft¹¹.

C. Methodology

A brief overview of the geometric properties for the UH-60A main rotor blade modeled in the LSAF calculations are given in Table 1. Detailed rotor chord distribution, airfoil distribution, and swept tip geometric parameters were taken from Figure 3 and Table 3 of Reference 7. The nonlinear twist distribution was taken from Figure 4 of Reference 7.

The model of the geometric blade planform was divided into 3 spanwise segments. The root cutout was set at 13.04 percent of the blade radius. The interior segment breaks were set at 92.86 percent of the blade radius, where the chord-length transitioned, and at 96.57 percent of the blade radius, where the swept tip began. The inboard segment was subdivided with 15 spanwise panels, with the panels being distributed using a half-cosine distribution to increase the density of panels towards the outboard end of the segment. The middle segment was subdivided with 2 panels, with both panels having equal spanwise spacing. The outboard segment was subdivided into 6 spanwise

Table 1: UH-60A main rotor properties.

Parameter	Value
Number of Blades	4
Radius (ft.)	26.83
Chord (in.)	20.76 / 20.965
Thickness (% chord)	9.5 / 9.4
Rotor Disk Area (ft. ²)	2261.5
Rotor Blade Area (ft. ²)	186.9
Solidity Ratio	0.0826
Blade tip sweep, aft	20°
Airfoils	SC1095/ SC1094R8
Nominal Rotor Speed (RPM)	258
Nominal Tip Speed (ft./sec.)	725

panels, with equal spanwise spacing used for all of the panels. The entire blade was subdivided with 5 chordwise panels, with a half-cosine panel distribution used to increase panel density towards the leading edge. The trailing edge blade tracking tabs were not included in the planform geometry input for LSAF. The flapping hinge offset ratio was set at 4.7 percent of the rotor radius. The coning angle was set at 2 degrees.

The ratio of two-dimensional to three-dimensional rise in drag divergence Mach number was specified as 1.00 to neglect thickness effects in Prouty's tip relief model.

Rollup of the tip vortices was specified to occur 30 degrees azimuthally behind the originating blade. The trailing wake filaments were divided into 36 increments per revolution. The inboard wake sheet was tracked for 1 revolution of the blade. The far wake filaments were truncated based at the default axial distance from the rotor disk. Scully's tip vortex core model was used, with the tip vortex core radius specified as 30 percent of the tip region chord. Tip vortex core bursting was not modeled.

The hover analysis was performed by using LSAF to conduct collective sweeps to calculate thrust coefficients. Iteration on thrust was performed for a specified collective until either successive thrust coefficient values converged to within an absolute tolerance of 1.2×10^{-7} , or an iteration limit of 1,000 was exceeded. Typically, solutions that exceeded the 1,000 iteration threshold were discarded.

D. Validation

For validation purposes, the LSAF model using the Clean airfoil section data was compared against data published in Reference 14. Sea level atmospheric conditions from the standard United States Atmospheric Model were assumed for the LSAF calculations. Figure 13 shows a plot figure of merit versus nondimensional thrust coefficient (C_T) divided by rotor solidity (σ). The blue squares represent data points calculated by LSAF. The blue line is a curve-fit using least-squares regression through the LSAF data, and was included as a visual aid. The red squares represent data scanned from Figure 10 of Reference 14. Figure 10 of Reference 14 is a compilation of UH-60A rotor hover figure of merit data from three helicopter aircraft experiments (with corrections) and three model-scale experiments (no scale-effect corrections).

From Figure 13, it may be seen that the LSAF data distribution is qualitatively similar to the data plotted from Reference 14. The LSAF data appears to be biased slightly higher than the Reference 14 data, though. This is attributed primarily to the fact that the LSAF model was not explicitly calibrated to account for parasitic power losses due to root end fittings, shafts, hinges, pitch links and other hub and control components. Based upon these factors, it was decided that the LSAF model was sufficiently valid for use in estimating performance differences between rotors using the three different sectional airfoil data sets.

E. Results and Discussion

For purposes of the evaluation reported here, hover performance was calculated at a high and hot atmosphere, equivalent to a pressure altitude of 4,000 feet and 95 degrees Fahrenheit outside ambient temperature. Relevant properties for these conditions are given in Table 1.

Figure 14 shows a plot nondimensional power coefficient (C_P) divided by rotor solidity versus the nondimensional thrust coefficient divided by rotor solidity for the main rotor blade using the three airfoil sectional data. Again, the solid lines were calculated from least-squares curve fits and were added to the plots as a visual aid.

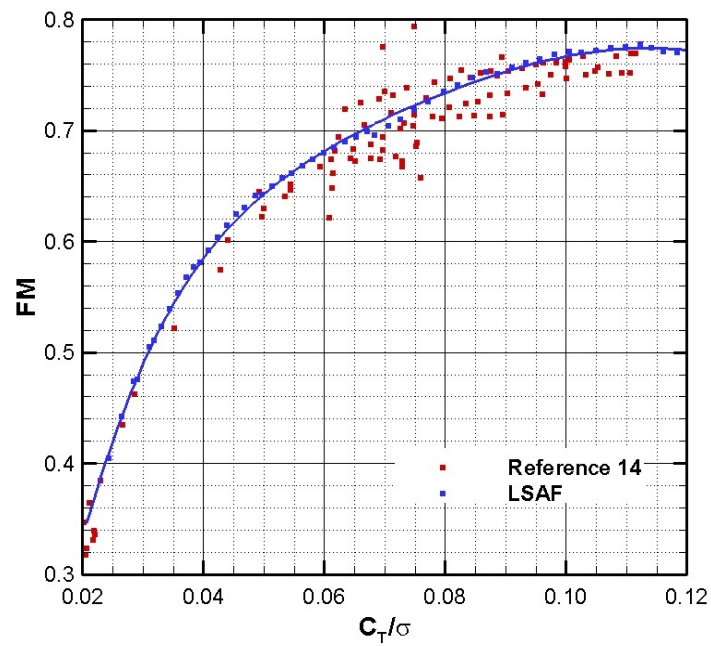


Figure 13. LSAF model validation.

Table 2: Atmospheric conditions.

Parameter	Value
Temperature (°F)	95
Pressure Altitude (ft.)	4,000
Density (slugs/ft ³)	1.920×10^{-3}
Speed of Sound (ft/sec.)	1,154.54

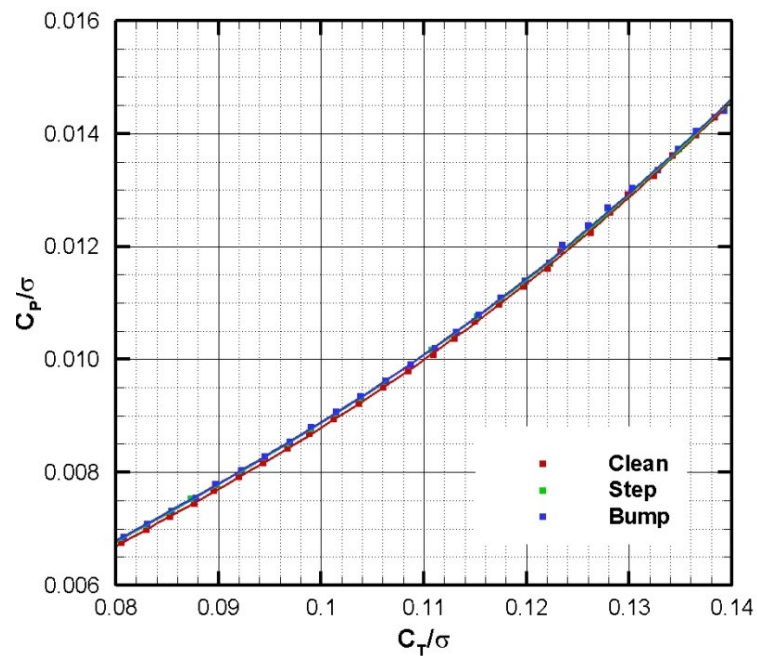


Figure 14. Power versus thrust.

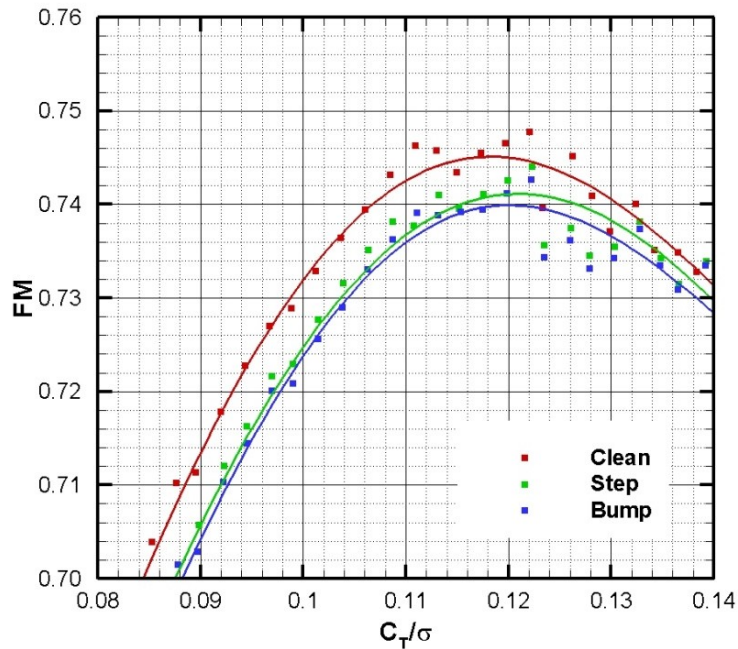


Figure 15. Figure of Merit versus thrust.

The graph scales have been selected to focus on the region of maximum rotor performance. However, the data distribution is still very close for the three rotor cases, though it may be discerned that the Clean airfoil rotor requires slightly less power than the Step or Bump rotors for a given thrust. However, this difference decreases with increasing thrust.

Figure 15 shows a plot of figure of merit versus the nondimensional thrust coefficient divided by rotor solidity. Figure of merit has enhanced the differences in performance between the three rotor cases in addition to illustrating the aerodynamic efficiency of the blades. The figure of merit of the rotors using the Clean airfoil sectional data is roughly 0.5 count in figure of merit higher than the other two plots in the region of peak figure of merit for the three blades. The figure of merit for the Step blade is approximately 0.1 count higher than the Bump blade. It may also be noted that the peak figure of merit values have been shifted to slightly higher thrust levels than the Clean airfoil rotor. However, from looking at the scatter in the experimental data from Reference 15 plotted in Figure 13, it is possible that the difference in performance between the coated and uncoated blades will lie within the “noise” of actual helicopter performance.

IV. Conclusion

Results into an investigation on the aerodynamic impact of erosion coatings applied to the leading-edge of a helicopter’s main rotor blade have been presented. Computational fluid dynamics was used to calculate tables of aerodynamic sectional data for a clean airfoil, an airfoil with a clean step termination edge, and an airfoil with an idealized bump meant to represent overspray of the protective coating onto the masking material. The airfoil sectional data for these three airfoil configurations were then used in a hover analyses to evaluate the impact of the coatings on a rotor’s integrated aerodynamic performance.

From the results of this investigation, the following conclusions may be drawn:

1. The presence of the erosion coatings did not significantly affect lift behavior in the linear region, and only slightly reduced the maximum lift coefficient for both Mach number conditions shown.
2. The erosion coatings significantly increased the profile drag of the coated airfoils, due to flow separation behind the termination edge, and thickening of the boundary layer aft of the termination edge. This increase was more pronounced for the lower Mach number than the higher Mach number.

3. The coating did significantly reduce the aerodynamic efficiencies of the coated airfoils in the angle of attack range approaching maximum lift. The difference in maximum efficiency was roughly equal between the Clean airfoil and the Bump airfoil for both Mach number conditions shown. However, the difference between the Clean and Bump configurations was roughly half for the higher Mach number than the lower Mach number.
4. The Bump and Step airfoils showed a roughly one-half count reduction in peak figure of merit when compared to the Clean airfoil. The Step airfoil blade showed slightly better performance than the Bump airfoil blade. However, these differences may lie within the “noise” of an actual helicopter’s performance.
5. Computational fluid dynamics and computationally inexpensive hover analysis tools can be used to evaluate performance trends for erosion protection coatings applied to rotor blades.

Acknowledgments

This work was supported in part by a grant of computer time from the Department of Defense High Performance Computing Modernization Program at the United States Army Engineer Research and Development Center Department of Defense Supercomputing Resource Center.

References

- ¹Ward, K. E., “The Effect of Small Variations in Profile of Airfoils,” NACA TN 361, 1931.
- ²Jacobs, E. N., “Airfoil Section Characteristics as Affected by Protuberances,” NACA TR 446, 1934.
- ³Jacobs, E. N., and Sherman, A., “Wing Characteristics as Affected by Protuberances of Short Span,” NACA TR 449, 1934.
- ⁴Cebici, T., “Effects of Environmentally Imposed Roughness on Airfoil Performance,” NASA CR-179639, 1987.
- ⁵Wilder, M. C., “Control of Unsteady, Separated Flow Associated with the Dynamic Stall of Airfoils,” NASA-CR-198972, 1995.
- ⁶Matheis, B. D., Huebsch, W. W., and Rothmayer, A. P., “Separation and Unsteady Vortex Shedding from Leading Edge Surface Roughness,” ADM201868, 2004.
- ⁷Bousman, W. G., “Aerodynamic Characteristics of SC1095 and SC1094 R8 Airfoils,” U.S. Army Aviation and Missile Research, Development and Engineering Center, Rept. NASA/TP-2003-212265, A-0309129, AFDD/TR-04-003, NASA Ames Research Center, CA, Dec. 2003.
- ⁸Smith, M. J., Potsdam, M., Wong, T.-C., Baeder, J., and Phanse, S., “Evaluation of CFD to Determine Two-Dimensional Airfoil Characteristics for Rotorcraft Applications,” U.S. Army Research, Development and Engineering Center, Rept. ADA480606, Redstone Arsenal, AL, Jun. 2004.
- ⁹Anderson, W. K., and Bonhaus, D. L., “An Implicit Upwind Algorithm for Computing Turbulent Flows on Unstructured Grids,” *Computers and Fluids*, Vol. 23, No. 1, pp. 1-21, 1994.
- ¹⁰LSAF, Lifting Surface Aerodynamics and Performance Analysis of Rotors in Axial Flight, Software Package, Ver. 2.XX, Computational Methodology Associates, Colleyville, TX. 2003.
- ¹¹Kocurek, J. D., Berkowitz, L. F., and Harris, F. D., “Hover Performance Methodology at Bell Helicopter Textron,” Preprint No. 80-3, *36th Annual Forum Proceedings*, American Helicopter Society, Washington, D. C., 1980.
- ¹²Kocurek, J. D., “A Lifting Surface Performance Analysis with Wake Circulation Coupled Wake for Advanced Configuration Hovering Rotors,” Ph.D. Dissertation, Dept. of Aerospace Engineering, Texas A&M University, College Station, TX, 1978.
- ¹³Kocurek, J. D., and Tangler, J. L., “A Prescribed Wake Lifting Surface Hover Performance Analysis,” *Journal of the American Helicopter Society*, Vol. 22, No. 1, 1977, pp. 24-35.
- ¹⁴Shinoda, P. M., Yeo, H., Norman, T. R., “Rotor Performance of a UH-60 Rotor System in the NASA Ames 80- by 120-Foot Wind Tunnel,” National Aeronautics and Space Administration, Rept. ADA480676, NASA Ames Research Center, CA, Jun. 2002.